ELSEVIER

Journal of Nuclear Materials 278 (2000) 173–185

journal of nuclear materials

www.elsevier.nl/locate/jnucmat

Temperature programmed decomposition of thorium nitrate pentahydrate

S. Dash [a], M. Kamruddin [a], P.K. Ajikumar [a], A.K. Tyagi [a], Baldev Raj [a,*], Santanu Bera [b], S.V. Narasimhan [b]

[a] *Metallurgy and Materials Group, Indira Gandhi Centre for Atomic Research, Kalpakkam 603 102, Tamil Nadu, India*
[b] *Water and Steam Chemistry Laboratory, BARC Facilities, Kalpakkam 603 102, Tamil Nadu, India*

Received 3 August 1999; accepted 18 October 1999

Abstract

Temperature programmed decomposition (TPD) of thorium nitrate pentahydrate has been studied using evolved gas analysis–mass spectrometry (EGA-MS) in the temperature range 300–1200 K. A thermogravimetric (TGA) investigation was also carried out in the same temperature range. Complexity of the TGA decomposition profile was resolved through use of EGA-MS data. The activation energies and pre-exponential factors were determined for various gas release stages from the fractional extent of decomposition plots. Residues left over after each decomposition stage were analysed using X-ray diffraction (XRD) and X-ray photoelectron spectroscopy (XPS). The XRD investigations revealed formation of a nanocrystalline thoria intermediate product, ultimately agglomerating to a microcrystalline phase. The XPS investigations indicated systematic alteration in the chemical environment around the thorium atom while the Th^{4+} oxidation state remained unchanged. This was further corroborated from the analysis of shake-up satellites of Th ($4f_{5/2}$) spectra. The O/Th ratios for various intermediate products were also determined.

PACS: 82.30Lp; 07.75.+h; 82.20Pm; 82.80.Pv; 81.70.Pg

1. Introduction

The thorium based fast reactor nuclear fuel cycle envisages thorex process flow sheet operations at the back end [1]. Product consolidation at this stage would require microwave denitration of thorium nitrate solution[2]. Mixed oxides like (U, Th)O_{2+x} can be prepared through co-denitration of respective nitrate salt solution followed by high temperature calcination. Various derivatives of $Th(NO_3)_4 \cdot 5H_2O$ are likely to be encountered in the denitration as well as calcination steps. Also the knowledge of single particle kinetics involved in decomposition process is absolutely essential for providing design inputs for the construction of macro-scale denitration apparatus. Both microwave powered as well as the conventional thermal ones would require this. In this context, the decomposition intermediates as well as the mechanistic pathway encountered in thermal and stoichiometric evolution of high specific surface thoria, the ultimate product of denitration, assumes significance.

A brief survey of literature revealed that a large number of derivative compounds of $Th(NO_3)_4$ have been studied by thermal analysis. These include chlorates [3], oxalates [4] and organic derivatives [5]. However, thermoanalytical study of $Th(NO_3)_4 \cdot 5H_2O$ has not been reported so far. In this backdrop, the following points were found to be worth investigating: (1) thermogravimetric study of temperature programmed stoichiometric transformations, (2) evolution of product stoichiometry in terms of oxygen to metal ratio, and (3)

* Corresponding author. Tel.: +91-4114 40234/40301; fax: +91-4114 40301/40360.
E-mail address: dmg@igcar.ernet.in (B. Raj).

0022-3115/00/$ - see front matter
PII: S0022-3115(99)00261-5

thermokinetic modeling of various conversion stages through application of non-isothermal kinetics. These points are addressed in the present investigation by studying temperature programmed decomposition of $Th(NO_3)_4 5H_2O$ using evolved gas analysis–mass spectrometry (EGA-MS), thermogravimetric analysis (TGA), X-ray diffraction (XRD) and X-ray photoelectron spectroscopy (XPS).

The EGA technique, based on mass spectrometry, has significant advantages in terms of sensitivity, specificity, fast response and multichannel detection capabiliity [6–8]. EGA-MS studies were conducted in the dynamic high vacuum to exclude recombination reactions. This enables correct sketching of mechanistic pathway. The TPD spectra obtained from EGA-MS was used to explain complex TGA weight loss profile. For this purpose, the TGA profile was deconvoluted to yield substages. Concomitant EGA profiles were used to explain stoichiometric transformations belonging to each TGA substage. Besides this, the EGA-MS data were also used to derive fractional extent of decomposition α and to deduce functional transform $f(\alpha)$ of non-isothermal solid state kinetic rate expressions [9,10]. This was used to assess the corresponding integral model function '$g(\alpha)$' [11–13]. Various stages of decomposition were found to comply with kinetic models based on random nucleation and diffusion [14]. The off-line characterization of residues left over after each NO_x (oxides of nitrogen: NO and NO_2) release stages was carried out by using powder XRD and XPS for studying structural and compositional variations resulting from the temperature programme. This was done to elucidate the mechanistic pathway leading to formation of thoria.

2. Experimental

GR grade $Th(NO_3)_4 \cdot 5H_2O$ powder samples procured from Merck KGaA, Germany were used in this study. The finely ground powders were examined by a polarised light optical microscope (OM) in the dark field reflection mode [15]. The particles showed a size distribution in 5–15 μm range [16]. Trace metallic constituents in this compound were determined using an ELAN 250 inductively coupled plasma mass spectrometer (ICP-MS) from SCIEX, Canada [17]. The samples were dissolved in spectroscopically pure reagents and sprayed to ICP by use of a peristaltic pump and Meinhard nebuliser [18]. Data were acquired by rapid scan mode. The instrument was calibrated using synthetic spectroscopically pure NBS traceable standards. Concentration of metallic impurities were found to be in μg/g level. These are presented in Table 1. The raw sample was also analysed by XRD and indexed to $Th(NO_3)_4 \cdot 5H_2O$ as reported in JCPDS [19].

150 mg of the sample was subjected to EGA-MS runs at 6 K/min heating rate in the temperature range 300–1200 K. The details of the EGA-MS experimental facility have been described elsewhere [20–22] and only a brief description will be furnished here. This facility consists of a high temperature (~1400 K), high vacuum programmable resistance furnace coupled to an ultra high vacuum (UHV, 10^{-10} mbar) chamber through a variable conductance molecular leak valve. The high vacuum chamber is pumped by a turbo molecular pump (TMP). The UHV chamber, housing the quadruple mass spectrometer and other metrological hardware like spinning rotor gauge (SRG) is pumped by a combined sputter ion-titanium sublimation pump (ISP). The ISP is backed by a separate TMP. The UHV chamber is also fitted with calibration gas inlets. A PC based software, developed in-house, executes real time multiple ion detection (MID) mass spectrometry. MID signals are plotted against absolute temperature of the sample to yield TPD spectra. The temperature of the uniformly spread thin sample layer is acquired by a calibrated K-type thermocouple through a PC based add-on card [23].

The TGA runs of $Th(NO_3)_4 \cdot 5H_2O$ were conducted in a polymer lab, UK make PL STA 1500 thermal analyser under Ultra High Pure (UHP, 99.99%) helium carrier gas flow of 40 ml/min. These runs were conducted at a heating rate of 6 K/min in the temperature range 300–1200 K. The experimental parameters for the TGA run were kept the same as the EGA-MS run to enable suitable comparison. Prior to acquisition of thermograms, the TGA/DTA machine was temperature calibrated by recording endothermal melting transitions of UHP metals like Sn, Zn and Al [24]. The thermo-

Table 1
Concentration of metallic impurities in $Th(NO_3)_4 \cdot 5H_2O$ as analysed by ICP-MS

Element	Concentration (μg/g)	Element	Concentration (μg/g)
Al	<15	Mn	<15
Ba	80	Mo	<15
Co	<15	Ni	<15
Cu	37	Pb	<15
Cr	<15	Sr	<15
Fe	22	Ti	<15
V	<15	Zn	<15

grams were also corrected for buoyancy and background [25]. Despite these precautions, minor discrepancies between TGA and EGA spectral temperatures were observed probably due to different sample environments.

For the purpose of condensed phase characterisation by XRD and XPS, the samples were heated till completion of various stages like dehydration and denitration. The temperature programme was terminated after completion of each stage. This was done by visually observing the EGA-MS spectra falling to the background upon interruption of a temperature programme. Such residues, withdrawn from the furnace after adequate cooling were labeled as follows:

A	raw samples (300 K)
B	post-dehydrated sample (525 K)
C	completion of initial Stage I denitration (550 K)
D	completion of Stage II denitration (650 K)
E	completion of final denitration (900 K)

These residues were transferred to XRD and XPS machines in sealed moisture proof containers.

Powder X-ray diffractograms of the sample and the residues were acquired by a Siemens D-5000 X-ray diffractometer equipped with a sample spinner. A thin layer of sample was spread uniformly on a zero background Si (9 1 1) substrate [26]. Using Cu-K_α as incident radiation, the scattered intensities were recorded in the 10°–70° 2θ span. Prior to acquisition of spectra, the instrument was properly aligned and checked for its figure of merit by conducting a run on α-quartz [27]. Spectral indexing were carried out with the help of JCPDS-ICDD sticks. However, in intermediates where no match could be found (i.e. B and C stages), ab initio indexing was carried out with the help of a least square fitting programme. This was corroborated by stoichiometric parameters derived from TGA and XPS runs. Scherrer formula [28] was used to determine the particle size of nanocrystalline intermediate.

XPS measurements were carried out with a VG ESCALAB MK 200X ESCA machine using an Al-K_α X-ray source (1486.6 eV) and a hemispherical mirror analyser which was operated on a band pass energy of 20 eV giving an analyser resolution of 0.4 eV. Here again a thin layer of powder sample was strapped to a 0.5 mm thick UHP indium metal foil. This was quickly loaded into the ESCA machine analysis chamber to avoid moisture ingress. Photoelectron emission from U (4f), O (1s) and C (1s) were recorded with about 0.1 eV/point. The binding energy was calibrated with Au ($4f_{7/2}$) photo electron peak at 84.0 eV with 1.6 eV FWHM for a specimen of Au film on Si substrate. Crystallographically pure thoria supplied by NIST was used as a reference standard. The metallic thorium value "($Th^{0+}4f_{7/2}$)" taken from the literature [29] was used by us to obtain core level chemical shifts of various intermediate residues. This became necessary as our repeated attempts to obtain an oxide-free metallic surface was unsuccessful. Also the present ESCA machine is not equipped with a metallic fracture stage. Such UHV cleaving normally reveals a pristine metallic surface.

3. Results and discussion

3.1. Kinetic analysis

The fractional extent of decomposition parameter $\alpha_{(T)}$ evaluated from the EGA data was used as an indicator of instantaneous condensed phase composition for the purpose of non-isothermal kinetic analysis of various decomposition stages [30]. The functional transform $f(\alpha)$, expressible as analytical functions is critically dependent on kinetic control mechanisms like random nucleation, diffusion and phase boundary motion [31]. Nucleation and growth phenomena become rate controlling when fast atomic migration pathways for continued formation of stable products exist [32], and the activation barrier to form product nucleus is easily overcome by strain energy available from defects and dislocations present in the interface. Once such pristine nuclei are formed on the defect sites, factors influencing their further rate of growth become decisive and manifest as controlling mechanisms. Nucleation and growth phenomena becomes rate controlling where there is continuous availability of defects and surfaces. In such cases rate of the chemical transformation alone controls the further growth of nuclei. Phase boundary motion and diffusional transport appear as controlling factors where a clear reactant/product interface with distinct crystallographic contrast gets established. If fast transfer paths are still available, reaction at the phase boundary becomes rate controlling. Otherwise diffusion control mechanisms manifest. Fig. 1 gives a schematic of various particulate conversion mechanisms. The mathematical expression used by us to obtain a least square correlation with experimental data involves $g(\alpha)$, the integral model function analytical expression. A list of such functions is given in Table 2. The expression runs as

$$\ln[g(\alpha)/T_2] = \ln(ZR/\beta E) - E/RT, \tag{1}$$

where T is the absolute sample temperature, Z the pre-exponential factor, β the heating rate, R the universal gas constant, and E the activation energy. The Arrhenius parameters E and Z are obtained from $\ln[g(\alpha)/T^2]$ vs $1/T$ plots through calculation of slopes and intercepts. In our procedure, we have computed $\ln[g(\alpha)/T^2]$ from measured α–T values and fitted it against theoretical $g(\alpha)$ expressions propounded for various kinetic

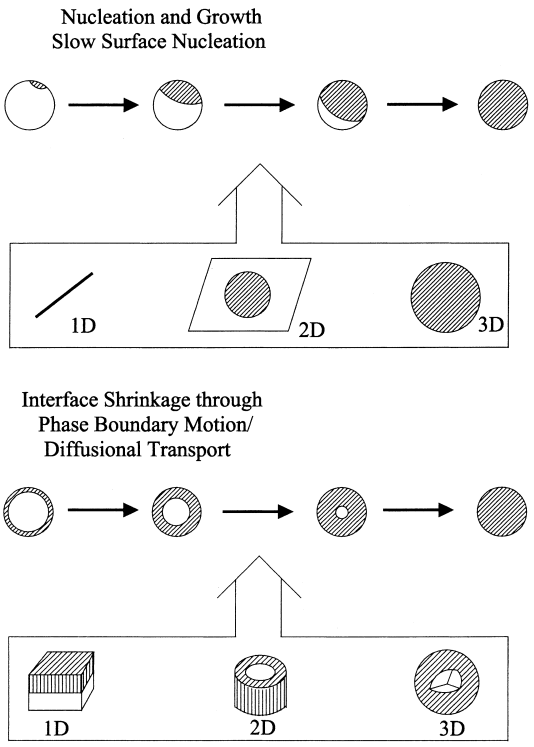

Fig. 1. Particulate conversion scheme in solid–gas decomposition reactions.

control models. The best fit has been regarded as the prevailing mechanism and is utilised for the evaluation of activation energy (E) and the pre-exponential factor Z [33].

3.2. EGA-MS studies

Fig. 2(a) shows the TPD Spectra of $Th(NO_3)_4 \cdot 5H_2O$ acquired at a heating rate of 6 K/min in the temperature range 300–1200 K. For the sake of comparison, the TGA weight loss spectra is superimposed on it. Corresponding EGA fraction release plots are shown in Fig. 2(b). Release of various gaseous species like H_2O ($m/e = 18$), NO ($m/e = 30$), O_2 ($m/e = 32$) and NO_2 ($m/e = 46$) have been recorded as a function of time and temperature. Although studies on EGA-MS and TGA were conducted in the temperature range 300–1200 K, the data are presented up to 900 K as no further spectral features were observed beyond this. The dehydration of the sample occurs in the temperature range 325–525 K. The EGA spectra, depicted in Fig. 2(a), appears to be bimodal. The decomposition reaction leading to evolution of NO, NO_2 and O_2 commences around 410 K and continues till 840 K. The decomposition initiation temperature is well below the completion temperature of dehydration. The decomposition process, involving the loss of NO, NO_2 and O_2 is referred as denitration. The abbreviation NO_x denotes simultaneous release of NO and NO_2 gases. The initiation of denitration appears concomitant with the final dehydration substage. The corresponding fraction release plots (Fig. 2(b)) show two dehydration stages and three denitration stages. Also mathematical deconvolution of dehydration and denitration revealed their sequential multistep nature. The deconvoluted spectra for dehydration and denitration are shown in Fig. 3(a) and (b), respectively. Dehydration substages AA′ and A′B showed an area ratio of 5:4. Desorption of the major fraction of crystalline water occurs in stage AA′. The maxima of water release peaks are centred at 387 and

Table 2
Nonisothermal, integral forms of kinetic expressions for heterogeneous solid-state reactions

Rate determining mechanism	Symbol	$g(\alpha) = \int_0^{\infty} d(\alpha)/f(\alpha)$
Nucleation and growth models		
Random nucleation approach		
(i) Mampel unimolecular law	A1	$-\ln(1-\alpha)$
(ii) Avrami–Erofeev nuclei growth	A2	$[-\ln(1-\alpha)]^{1/2}$
(a) 2-dimensional growth	A3	$[-\ln(1-\alpha)]^{1/3}$
(b) 3-dimensional growth		
(iii) Branching nuclei		
Prout Tompkins branching nuclei	A4	$\ln[\alpha/(1-\alpha)]$
Decelerating rate equations based on diffusion		
(i) Parabolic law 1-dimensional transport	D1	$\alpha^2/2$
(ii) 2-dimensional diffusion	D2	$(1-\alpha)[\ln(1-\alpha)] + \alpha$
(iii) 3-dimensional diffusion (Jander–Mech)	D3	$1.5[1-(1-\alpha)^{1/3}]^2$
(iv) 3-dimensional diffusion (Ginstling–Brounshtein)	D4	$1.5[1-2\alpha/3-(1-\alpha)^{2/3}]$
Phase boundary movement		
(i) 1-dimensional (zero order)	R1	α
(ii) 2-dimensional (cylindrical symmetry)	R2	$2[1-(1-\alpha)^{1/2}]$
(iii) 3-dimensional (spherical symmetry)	R3	$3[1-(1-\alpha)^{1/3}]$

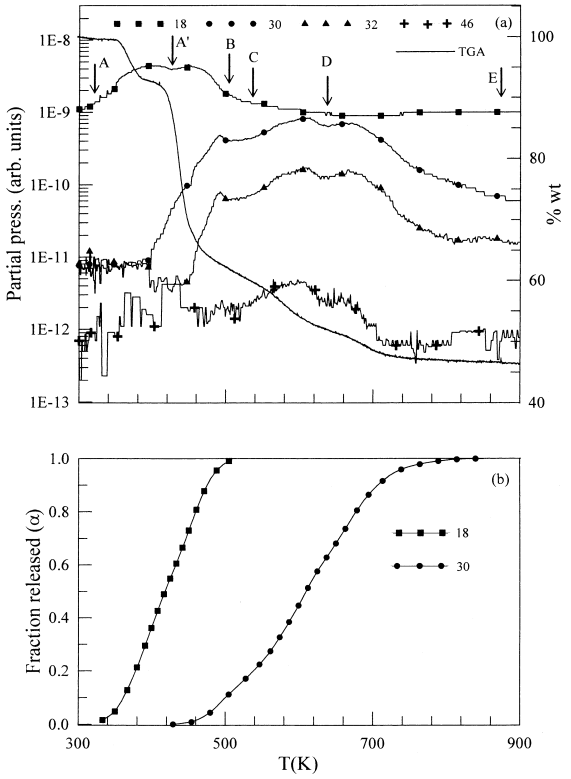

Fig. 2. (a) EGA-MS Spectra of $Th(NO_3)_4 \cdot 5H_2O$ superimposed with TGA weight loss profile. (b) Fraction release $\alpha_{(T)}$–T plots derived from EGA-MS data.

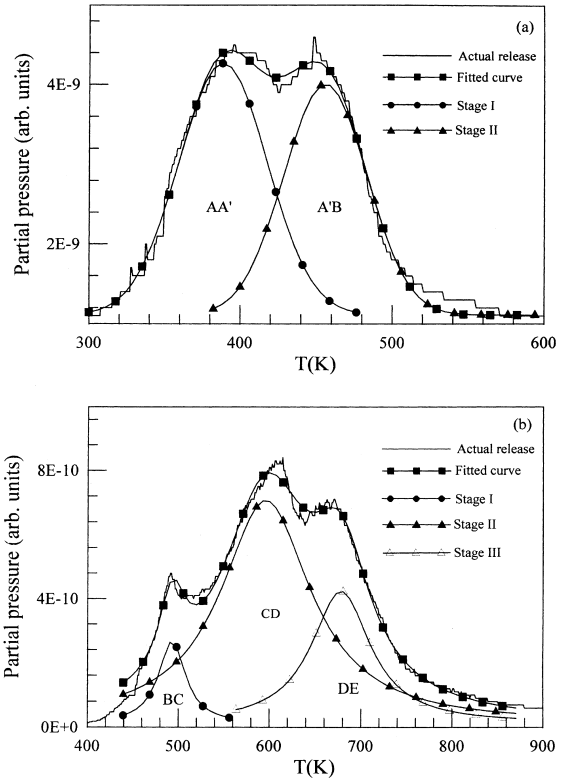

Fig. 3. (a) Deconvoluted dehydration profile. (b) Deconvoluted denitration profile.

458 K, respectively. Similar deconvolution of overlapping denitration stages revealed three different substages, namely, BC, CD and DE. The EGA–MS peak areas pertaining to these sub stages bear proportionality BC:CD:DE = 1:9:3.5. This indicates varying degree of NO_x loss. The inflexion temperatures for maximum release rates are 490, 600 and 678 K, respectively. These substages are clearly depicted in Fig. 3(b).

The kinetic evaluation procedure was adopted to establish kinetic control regimes for various dehydration and denitration stages and to determine associated Arrhenius parameters like activation energy E and pre-exponential factor Z. Kinetic correlation diagrams depicting various rate controlling mechanisms are shown in Fig. 4. The values of E and Z are given in Table 3. The initial dehydration stage AA′ was found to be controlled by Random Nucleation (RN). This nucleation and growth limited phenomena is due to desorption of highly labile uncoordinated librational water. In thorium nitrate pentahydrate, the oxygen atoms of three water molecules along with eight from four bidentate nitrate groups are coordinated directly to the central metal cation forming a highly irregular coordination polyhedron [34]. These three water molecules are also structurally different. The two exterior water molecules reside outside the coordination sphere and desorb immediately after heating is started due to weak binding. The final dehydration stage A′B involves loss of a part of the cation coordinated water. This amounts to 80% of the initial release. The remaining water molecules are probably carried forward beyond the dehydration stage. The kinetics of this later dehydration stage are governed by three-dimensional Jander–Mech diffusional rate expression (Fig. 4(b)). This mechanism manifests due to product barrier layer formation.

The denitration of the compound occurs in the temperature range 410–840 K. This stage is marked with concomitant release of NO ($m/e = 30$), O_2 ($m/e = 32$) and NO_2 ($m/e = 46$). This spectral appearance is characteristic of the nitrate group cleavage. Deconvolution of EGA–MS spectra (Fig. 3(b)) reveals three distinct NO_x release stages. The initial release spans 410–550 K. The maximum release occurs around 490 K. This denitration stage, termed as BC, is concomitant with the final dehydration stage. Comparison of peak areas indicate 7.5% of the total NO_x is released in this stage. The kinetic control of this stage also shows governance by the Jander–Mech 3-dimensional diffusion mechanism

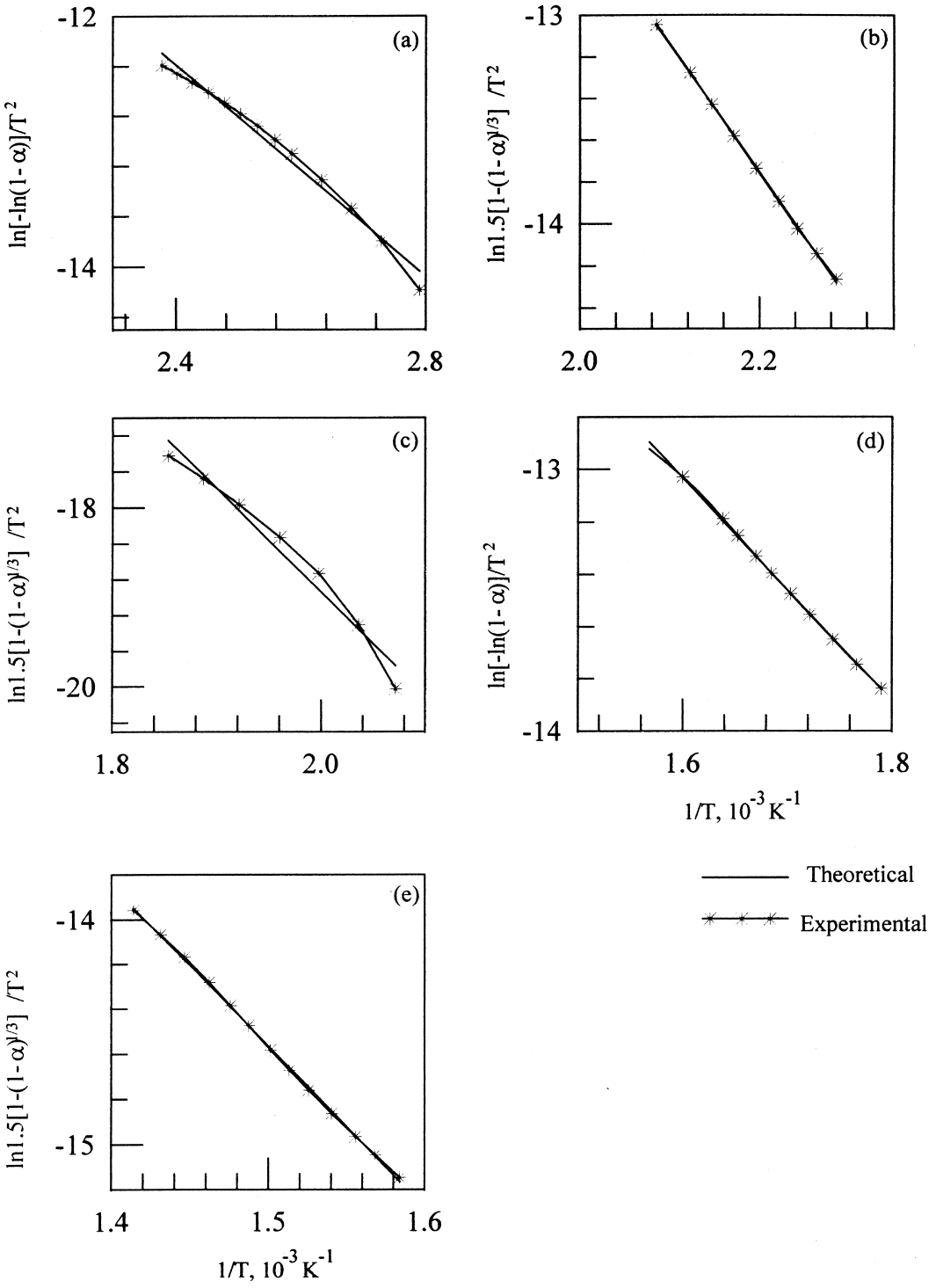

Fig. 4. Kinetic correlation plots showing prevalence of various rate controlling mechanisms. * Experimental line, least square fitted line. (a) Stage I dehydration (AA′) showing A1 control. (b) Stage II (A′B) showing D3 control. (c) Stage I denitration (BC) showing D3 control. (d) Stage II denitration showing A1 control. (e) Stage III denitration showing D3 control.

Table 3
Reaction mechanism, corresponding correlation coefficients, activation energy and pre-exponential factors for various dehydration and denitration stages of decomposition of $Th(NO_3)_4 \cdot 5H_2O$

Stages	Mechanism	Correlation coefficient	Activation energy (kJ/mol)	Pre-exponential factors (s^{-1})
Dehydration				
Stage I (AA′)	Random nucleation	0.991	34.246	1.978×10^3
Stage II (A′B)	Jander	0.999	50.792	2.685×10^3
Denitration				
Stage I(BC)	Jander	0.983	95.486	3.871×10^6
Stage II (CD)	Random nucleation	0.999	35.363	50.47
Stage III (DE)	Jander	0.999	59.385	9.11×10^2

(Fig. 4(c)). The Stage II denitration is the most dominant NO_x release stage. It peaks around 600 K and roughly covers 66.5% of the NO_x release. This stage is designated as CD. The kinetics of Stage II denitration indicate control by random nucleation process (Fig. 4(d)). Reappearance of the RN mechanism can be attributed to a possible structural collapse leading to generation of an X-ray amorphous phase. This is a consequence of hydrogen bond loss. Such phenomena have been observed by us in many other H-bonded solids like alum [35]. The final denitration step (Stage III) pertains to decomposition of residual nitrate groups. This stage is designated as DE which spans 650–840 K. It is peaked around 680 K. Nearly 26% denitration occurs in this stage. The kinetics are governed by 3-dimensional Jander–Mech rate expressions (Fig. 4(e)).

The multistep denitration can be explained on the basis of crystallographic inequivalence of nitrate oxy anion. The N–O and Th–O bond distances are different for various nitrate groups. The hydrogen bonding scheme for various functional groups are different. This leads to different levels of instability of atoms as evidenced from varying amplitudes of thermal vibration [36].

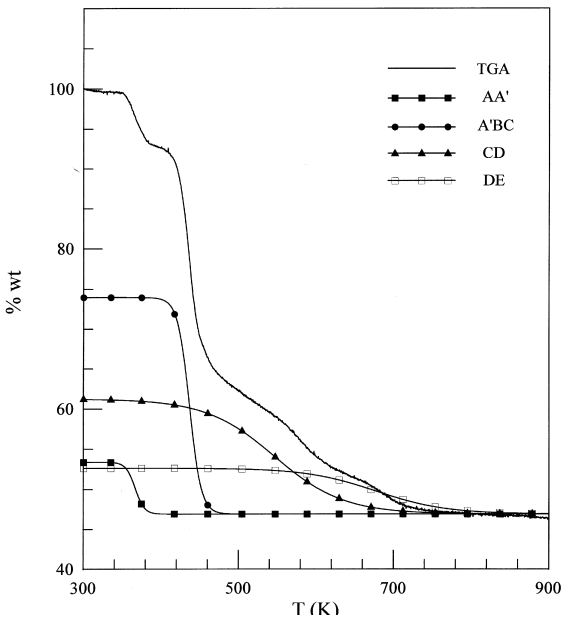

Fig. 5. TGA weight loss profile for $Th(NO_3)_4 \cdot 5H_2O$ at 6 K/min deconvoluted to show 4 substages. AA′: stage I dehydration, A′BC: stage II dehydration and stage I denitration, CD: stage II denitration, DE: stage III denitration.

3.3. TGA studies

The complex multimodal TGA weight loss profile was superimposed on the EGA profile. This profile was deconvoluted to reveal four distinct weight loss stages as shown in Fig. 5. The AA′ stage spans the temperature range 350–400 K. This corresponds to a weight loss of 6.3%. In this regime, the corresponding EGA-MS spectra depicts water release. Hence, the above weight loss is explainable on the basis of loss of two molecules of water from the formula molecular unit. The next weight loss stage A′BC spans 400–485 K corresponding to a weight loss of 27.92%. This stage has an inflexion at 436 K. The EGA-MS spectra in this region depict concomitant dehydration as well as denitration. Hence, the weight loss corresponds to release of two molecules of water, two molecules of each gaseous species constituting NO_x and one molecule of O_2. The weight loss stage CD as revealed from the corresponding EGA-MS spectra turns out to be a denitration stage only. This stage spans 500–700 K with an inflexion at 550 K. A weight loss of 14.6% is incurred at this stage. The final weight loss stage is again a purely denitration step involving decomposition of residual nitrate. This stage spans 600–800 K and has inflexion at 683 K. A weight loss of 4.6% was observed in this stage. The TGA inflexion temperatures were found to be lower compared to EGA-MS values. The reason can be attributed to much more uniform distribution of temperature of the sample in helium gas environment due to better thermally conductive atmosphere [37].

3.4. XRD studies

The starting compound as well as the condensed phase residues that were collected at various times during the temperature programme were subjected to powder XRD analyses to study crystallo-chemical transformations. The compounds are marked as A, B, C, D and E. A refers to untreated initial compound. B, C, D and E are residues withdrawn from the EGA furnace at 525, 550, 650 and 900 K, respectively. Powder XRD patterns are depicted in Fig. 6. The initial sample 'A' as reported [34,36] consists of a non-centrosymmetric orthorhombic unit cell having space group Fdd2 and eight formula molecular units of $Th(NO_3)_4 \cdot 5H_2O$. The thorium atom has 11 oxygen neighbours arranged in a highly unsymmetrical way with respect to polar directions. Bidentate nitrate groups contribute eight oxygen sites, while the remaining three are provided by water oxygen. The Th–O (water) distance is shorter than the Th–O (Nitrate) distance. There are two distinctly different types of hydrogen bonds, one is a fairly strong water–water hydrogen bond and the other one is a weak water–nitrate hydrogen bond. The structural frame work is clearly based on hydrogen bonding with fairly large unit cell dimensions having lattice parameters $a = 1.1182$, $b = 2.7873$ and $c = 1.0573$ nm. The weak H-bond probably pertains to bonding of exterior water molecules which appear as librationally attached functional group in the infrared spectrum at 3440 cm^{-1} [38,39].

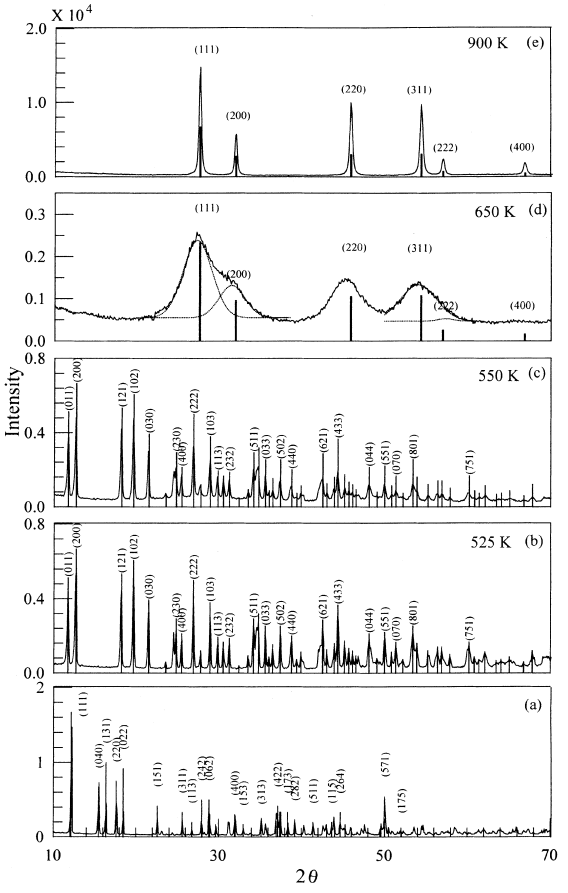

Fig. 6. Powder X-ray diffraction pattern for: (a) original $Th(NO_3)_4 \cdot 5H_2O$: sample A; (b) $Th(OH)_{1+x}(NO_3)_2$: residue – B; (c) $ThO(NO_3)_2$ – residue C; (d) nanocrystalline thoria: – residue D (X-ray amorphous $ThO_{1+x}(NO_3)_{2-y}$ phase is not seen; (e) microcrystalline thoria – residue E.

The nitrate oxy anion ligands are also not unique. Studies by Bagnal et al. [40] indicate that there are two identical ligands in equatorial location where two others hang down from the equatorial plane. The nitrate group symmetry also gets distorted from D_{3h} to C_{2v} due to H-bonding [41]. Thus, the high degree of inequivalence of water molecules and nitrate ligands render complexity to the temperature programme driven gaseous species evolution process.

Transition of the sample from Stage A to Stage B is accompanied with concomitant release of water and NO_x. The reason can be attributed to similarity in bonding patterns for the water and the nitrate groups [34]. This is also reflected in the near similar thermal motion amplitudes between certain water oxygen and nitrate oxygen [36]. As reported in the case of ionic nitrates [42] and evidenced from stiochiometric balance, a hydrolysed intermediate $Th(OH)_{1+x}(NO_3)_2$ with $x \sim 1$ is formed in this stage. It is termed as compound 'B'. Fig. 6(b) shows the diffractogram. Such hydrolysed intermediates have been reported earlier in the decomposition of ionic nitrates like $UO_2(NO_3)_2 \cdot 6H_2O$ [42]. Corroborative evidence to be furnished latter in this study through XPS investigation also points towards this conclusion. Existence of similar hydroxylated compounds i.e. $Th(OH)_2SO_4$ [43] and $Th(OH)_2CrO_4 \cdot H_2O$ [44] have been reported. Such hydroxy nitrate intermediates result from the carry over of residual water beyond the dehydration stage. It has been reported that, in certain other lanthanide homologues of this compound, dehydration and denitration stages often overlap [45]. As no matches were found in the JCPDS-ICDD, structural pattern determination from the powder diffraction data was carried out through a least square fitting procedure. The compound was indexed to an orthorhombic unit cell having lattice parameters $a = 1.399$ nm, $b = 1.243$ nm and $c = 0.951$ nm. The procedure allowed indexing of most of the prominent intensity lines with a reasonably good figure of merit. It is noticed that, compared to the unit cell volume of pristine $Th(NO_3)_4 \cdot 5H_2O$, the hydroxylated intermediate showed considerable volume reduction. The reason can be attributed to release of various functional groups leading to structural simplification. Larger ionicity of

the hydroxyl group is also a contributing factor for the structural contraction.

The stage C residue at 550 K (Fig. 6(c)) indicated almost identical powder diffraction pattern except for the reduced intensities. At this stage, the hydroxylated groups are removed and ionicity gets reduced. Stoichiometric balance indicates formation of an oxy nitrate intermediate $ThO(NO_3)_2$ with similar orthorhombic lattice. Such oxy nitrate phases have been reported in the thermal decomposition of rare earth nitrates [46]. The diffraction line locations in the oxy nitrate phase is analogous to the hydroxy nitrate phase, but there is systematic decline in the diffraction line intensities. The splitting depth of certain diffraction lines are also reduced. Thus transition to a more symmetric phase is indicated, perhaps due to loss of highly ionic hydroxyl groups.

The residue at 650 K shows broad Bragg peaks. Mathematical deconvolution of spectra indicated formation of ThO_2 having $Fm\bar{3}m$ space group. Fig. 6(d) shows the diffractogram. Stoichiometric estimate indicate formation of the $ThO_{1+x}(NO_3)_{1-y}$ type of compound, which is probably X-ray amorphous. Due to complete loss of hydrogen bonding, the compound undergoes amorphosization. At this stage, nucleation and growth of nanocrystalline ThO_2 from an amorphosised intermediate is noticed. This is also evidenced from random nucleation dominated kinetics. To calculate the particle size of the nanocrystalline intermediate, Scherrer formula based on X-ray line profile broadening was utilised [28]. The formula is given as

$$t = 0.9\lambda/\beta \cos\theta_B, \tag{2}$$

where t indicates the particle size in nanometres and λ the incident X-ray wavelength. In this case, it was taken to be 0.154183 nm, which is the weighted average of Cu-$K_{\alpha 1}$ and Cu-$K_{\alpha 2}$ lines. β is a radian measure of full width at half maximum (FWHM) and $2\theta_B$ is the angle subtended at maximum intensity. FWHM in this case was calculated after subtraction of the X-ray machine contribution to broadening. This analysis revealed an approximate particle size range of 2.5–3.0 nm.

Advancement of the temperature programme to 900 K (residue E) resulted in complete decomposition of X-ray amorphous residual nitrates and coagulation of nanocrystallites into microcrystalline thoria having a fluorite structure and $Fm\bar{3}m$ space group. All the lines seen in the diffractogram (Fig. 6(e)) could be indexed to those reported in the literature [47].

3.5. XPS studies

Keeping the structural information received from the XRD data as background, the chemical environment around thorium was probed by the XPS to confirm the mechanistic pathway involved in the conversion of $Th(NO_3)_4 \cdot 5H_2O$ to ThO_2. Also alteration in the O/Th ratio driven by the temperature programme was mapped. Crystallographically pure ThO_2 was used as a reference material. $Th(4f_{7/2})$, O(1s) and C(1s) photoelectron peaks were recorded. The thorium and oxygen photo-peaks belonging to the various decomposition stages are shown in Figs. 7 and 8, respectively. It is known that the $Th(4f_{7/2})$ photoelectric peak in pure thorium metal occurs at 333.05 eV [29]. ThO_2 having +4 oxidation state for Th, the only oxidation state of Th, is indicated in the XPS spectrum as the characteristic $4f_{7/2}$ peak occurring at 333.6 eV with a satellite at 7.2 eV ahead of the main peak. The value from our experiments is found to be lower than 334.6 eV reported by Veal et al. [48]. In ThO_2, multiplication of appropriate sensitivity factors yielded a O/Th ratio of 2.2 [49].

Variable oxidation state, characteristic of early actinides does not manifest in thorium due to absence of 5f electron. The hybridised bonding bands with f-character, observed normally in other actinide compounds, is

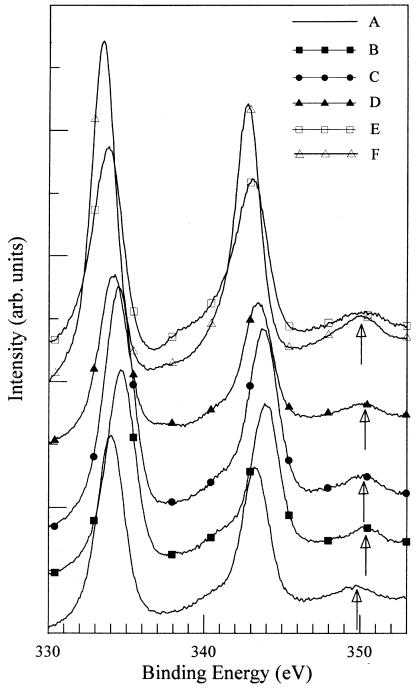

Fig. 7. Th (4f) photoelectric peaks at different stages of decomposition: (a) original $Th(NO_3)_4 \cdot 5H_2O$ – sample A; (b) $Th(OH)_{1+x}(NO_3)_2$ – residue B; (c) $ThO(NO_3)_2$ – residue C; (d) nanocrystalline thoria – residue D with X-ray amorphous $ThO_{1+x}(NO_3)_{2-y}$ phase; (e) microcrystalline thoria – residue E; (f) Stage E residue after ion beam exposure. Arrow marks indicate satellite peak positions.

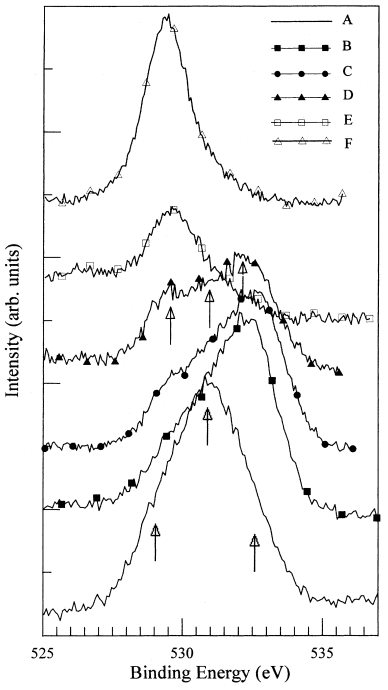

Fig. 8. Oxygen (1s) photoelectric peaks at different stages of decomposition: (a) original $Th(NO_3)_4 \cdot 5H_2O$ – sample A; (b) $Th(OH)_{1+x}(NO_3)_2$ – residue B; (c) $ThO(NO_3)_2$ – residue C; (d) nanocrystalline thoria – residue D with X-ray amorphous $ThO_{1+x}(NO_3)_{2-y}$ phase; (e) microcrystalline thoria – residue E; (f) stage E residue after ion beam exposure. Arrow marks indicate oxygen peak positions.

absent here. Chemical bonding interactions through the ligand s and p orbitals are restricted to the Th $6d^27s^2$ orbitals only [50]. In all our investigations of $Th(NO_3)_4 \cdot 5H_2O$ and its derived intermediate stages the C(1s) peak always appeared above 290 eV indicating charging, caused by the insulating nature of the materials. Hence, appropriate charge correction procedures were used for arriving at correct binding energy values. In stage A, a sample of pristine compound $Th(NO_3)_4 \cdot 5H_2O$, the Th($4f_{7/2}$) peak was observed at 334.2 eV with FWHM 2.1 eV. Compared to 333.0 eV for Th^{0+}, a chemical shift of 1.2 eV is seen. Th in this compound is in the +4 state. In the +4 oxidation state of thorium, the $4f_{5/2}$ satellite peak occurs at 6.0 eV ahead of the main peak. The satellite signature is attributed to the charge transfer excitation from occupied ligand orbitals to an empty or partially filled metal electronic level [51]. In the case of the Th compound, such excitation involves optical transitions from bonding band to the conduction band minima . Binding energy in this case, compared to ThO_2, is 0.6 eV higher. The effective charge state of the eleven atom coordinated thorium in this compound is higher due to the presence of Th ← O–N and Th ← O–H type of bondings. The O(1s) peak of this compound was found to be a convolution of three different photo peaks arising out of the three distinctly different oxygen chemical environments. The peak at 532.5 eV is due to the O–H bond, 531.5 eV due to the O–N bond and 529.5 eV due to the Th–O bonded oxygen.

The stage B residue at 525 K, corresponding to the hydoxy nitrate intermediate, yielded a Th ($4f_{7/2}$) photo-peak at 334.8 eV with a satellite signature at 6.2 eV ahead of the $4f_{5/2}$ photo-peak. The increase in the spectral chemical shift can be attributed to the high ionic nature of hydroxyl groups contributing more towards effective charge on the thorium atom, although the satellite position and appearance indicated continued +4 oxidation state of the thorium. A change in the satellite peak area points towards subtle redistribution in the valence band. Here also, the O(1s) signal indicated continued presence of O–H, O–N and O–Th oxygen environment. A sizeable increase in the O–H group related photo-peak area points towards hydroxylation of the pristine compound. Reduction in the total oxygen peak area occurs due to desorption of oxygen bearing groups resulting from the dehydration and the denitration processes.

The Th ($4f_{7/2}$) photo peak in stage C residue (550 K) occurs at 334.6 eV with a $4f_{5/2}$ satellite 6 eV ahead of the main peak. Reduced chemical shift results from removal of hydroxyl groups and formation of an oxy nitrate phase. The total oxygen peak area nearly remained the same as Stage C. However, the O–H peak area as well as the O–N peak areas declined whereas the Th–O peak area increased. Continued occurrence of the O–H type of bonding indicate a minor carryover of stage B compound.

Stage D residue obtained after reaching 650 K consisted of carry over of stage C oxy nitrate residue with a significant portion of it decomposed to yield nanocrystalline thoria. The compound can be designated as $ThO_{1+x}(NO_3)_{1-y}$ which is continually converted to ThO_2 at the expense of residual nitrate. Th $4f_{7/2}$ peak appeared at 334.2 eV with a $4f_{5/2}$ satellite 6.9 eV ahead of the main peak. The satellite appearance of approximately 7 eV indicates the onset of thoria formation. Chemical surrounding of oxygen is dominated by the Th–O type of bonding. Persistence of minor O–N and O–H peak areas indicate carry over of earlier phases.

Stage E residue obtained after attainment of 900 K yielded a Th($4f_{7/2}$) peak at 333.9 eV with a satellite at 7.3 eV ahead of the main Th($4f_{5/2}$) peak. This was compared with our XPS spectrum of crystallographically pure thoria which yielded a Th($4f_{7/2}$) peak at 333.6 eV with a $4f_{5/2}$ satellite peak 7.4 eV ahead. The O(1s) peak was almost singular with a peak maximum at 529.8 eV. This is close to the standard thoria value of

Table 4
Photoelectric peak position for thorium and oxygen electronic levels

Peak (eV) (area)	$Th(NO_3)_4 \cdot 5H_2O$	Residue B (525 K)	Residue C (550 K)	Residue D (650 K)	Residue E (900 K)	Crystallographic ThO_2
Th ($4f_{7/2}$)	334.2	334.8	334.6	334.2	333.9	333.6
Principal peak	(71855.4)	(72748.9)	(90115.6)	(74323.2)	(94363.7)	191260.2
[FWHM]	[2.03]	[2.2]	[2.34]	[2.24]	[2.37]	[1.8]
$4f_{5/2}$ main peak	343.5	344.1	344.00	343.6	343.1	343.0
	(44201.1)	(46951.8)	(63302.2)	(51410.5)	(73391.8)	145401.8
	[2.03]	[2.06]	[2.3]	[2.23]	[2.52]	
Satellite	349.5	350.3	350.5	350.5	350.4	350.4
	(4420.1)	(3229.6)	(6959.5)	(3588.2)	(7879.3)	14797.9
	[1.93]	[1.61]	[2.69]	[2.23]	[2.83]	–
O (1s)	531.1	532.10	532.00	531.7	529.8	529.7
Total area	(51181.1)	(39287.0)	(38874.6)	(22373.1)	(24420.2)	37417.2
	[3.77]	[3.46]	[3.95]	[4.16]	[3.11]	[2.32]
Decon. area	(9887.8)	(20892.5)	(18679.3)	(10184)	–	–
532.5	[1.97]	[1.97]	[1.97]	[1.97]		
531.3	(925970.0)	(15584.0)	(13857.0)	(9740.1)	–	–
	[2.1]	[2.1]	[2.1]	[2.1]		
529.5	(15184.5)	(5396.3)	(6139.2)	(5159.6)	–	–
	[2.29]	[2.29]	[2.29]	[1.9]		
O/Th ratio	17[a]	6.5	5.27	3.9	2.8	2.2

[a] Molecular structural value.

529.7eV. The signature of O–H and O–N environments are not detected at this stage. However, FWHMs of characteristic peaks of stage E residue were broader than the corresponding values for standard ThO_2. The reason may be attributed to undetectable quantities of phases carried over from the earlier stages. Broad FWHMs are caused by the convolution of signals from various carry over phases. To get rid of unstable carry over intermediate phases, the Stage E residue was impinged with an Ar^+ ion beam operating at 3 keV and 1 μA current inside the ESCA machine. After brief sputtering, the thorium and oxygen peak positions as well as their FWHMs showed perfect matches with standard ThO_2 values. The reason can be attributed to the ion beam induced dissociation of left over O–H and O–N bearing functional groups.

It can be summarised that though the oxidation state of Th remained in the + 4 state, which is attributable to the non-bonding characteristic of 5f orbitals and the absence of electron occupancy, the chemical surrounding continually altered throughout the thermal ramping. Continuous valence band shake-up is evidenced from satellite FWHM and peak area changes. Results from XPS studies are summarised in Table 4 along with O/Th values. These values indicate a systematic decline in oxygen content of the material. Based on the above observations and inferences drawn from the EGA-MS, TGA and XRD studies, the kinetic pathway for the TPD of $Th(NO_3)_4 \cdot 5H_2O$ runs as follows:

A	$[Th(NO_3)_4 \cdot 3H_2O] \cdot 2H_2O$	300 K
	A1↓	
A′	$Th(NO_3)_4 \cdot 3H_2O$	425 K
	D3↓	
B	$Th(OH)_{1+x}(NO_3)_2$	525 K
	D3↓	
C	$ThO(NO_3)_2$	550 K
	A1↓	
D	$ThO_{1+x}(NO_3)_{1-y}$	650 K
	D3↓	
E	ThO_2	900 K

4. Conclusion

The TPD of $Th(NO_3)_4 \cdot 5H_2O$ has been studied by EGA-MS, TGA, XRD and XPS in the temperature range 300–1200 K. The EGA studies indicated a sequential nature of dehydration and denitration phenomena. The kinetics of various release stages, as evaluated from EGA-MS data, indicated prevalence of surface desorption based random nucleation control as well as diffusional limitations. Arrhenius parameters like activation energy

and pre-exponential factors could be determined. The complex TGA weight loss profile was mathematically deconvoluted, and various stages were matched to dehydration and denitration steps observed in the gas release signal of the EGA–MS spectra. XRD investigations revealed sequential dehydration and intermediate phase formation. Hydroxy nitrate and oxy nitrate phases observed in XRD data were corroborated by XPS studies. Nanocrystalline thoria formed from conventional amorphosised thorium oxy nitrate was confirmed from X-ray line profile broadening analysis. XRD analysis revealed structural evolution of microcrystalline thoria from a nanocrystalline intermediate phase through thermal growth. XPS investigations revealed unchanging +4 oxidation state of thorium in various thermally derived intermediate stages. Variation in chemical shift along with satellite position indicates continually changing chemical coordination around the thorium atom. Also, alteration in FWHM of the main as well as the satellite peaks indicate convolution of photo-peaks of various carry over intermediate phases. The signature of these unstable carry over intermediates could be completely obliterated through ion beam exposure. The oxygen–metal ratio calculated from XPS data also showed systematic decline with ascending temperature.

Mixed oxide fuel fabrication procedure, envisaged in the thorium based fuel cycle, can reliably use temperature window available from this study to synthesise thoria nanoparticles. Such powders having exceptionally high specific surface would ensure superior microhomogeniety when mixed with the oxides of uranium. This in turn, may improve the irradiaion perfomance of the fuel pellet. The temperature dependent conversion parameters obtained from the study of single particle kinetics is an essential pre-requisite for designing the macro-scale denitration utilities. Also the knowledge of gas release rates will aid in appropriately sizing the downstream gas management equipment for NO_x abatement.

Acknowledgements

The authors acknowledge Dr G.V.N. Rao, Dr Goutam Ghosh and Shri V.S. Sastry for acquisition of powder XRD patterns and subsequent discussions. We are grateful to Dr V. Sridharan for TGA runs, Shri J. Jayapandian and Dr B. Purniah for instrumentation support. Shri K. Varatharajan's assistance in optical microscopy and Shri R.K. Prabhu's help on ICP-MS are also acknowledged.

References

[1] G.R. Choppin, J. Rydberg, Nuclear Chemistry: Theory and Applications, Pergamon, Oxford, 1980, p. 531.
[2] B.J.F. Palmer, L.E. Bahen, A. Celli, Am. Ceram. Soc. Bull. 63 (1984) 1030.
[3] R.K. Agarwal, S.C. Rastogi, Thermochim. Acta 62 (1983) 379.
[4] M.T. Aybers, J. Nucl. Mater. 252 (1998) 28.
[5] A.K. Srivastava, R.K. Agarwal, Thermochim. Acta 68 (1983) 121.
[6] P.K. Gallaghar, Thermochim. Acta 26 (1978) 175.
[7] P.K. Gallaghar, J. Thermal Anal. 25 (1982) 7.
[8] H.G. Langer, in: E.J. Elving (Ed.), Treatise on Analytical Chemistry Part I, 2nd Ed., vol. 12, Wiley, New York, 1983.
[9] D. Price, D. Dollimore, N.S. Fatemi, R. Whitehead, Thermochim. Acta 42 (1980) 323.
[10] D. Price, N.S. Fatemi, D. Dollimore, R. Whitehead, Thermochim. Acta 94 (1985) 313.
[11] A.W. Coats, J.P. Redfern, Nature 201 (1964) 68.
[12] E.S. Freeman, B. Carroll, J. Phys. Chem. 62 (1958) 394.
[13] A.M. Gadalla, Thermochim. Acta 95 (1985) 179.
[14] M.E. Brown, D. Dollimore, A.K. Galway, in: C.H. Bamford, C.F.H. Tipper (Eds.), Reactions in the Solid State, Elsevier, Amsterdam, 1980.
[15] H.E. Knechtel, W.F. Kindle, J.L. McCall, R.D. Buchheit, in: Taylor Lyman (Ed.), Metals Handbook, vol. 8, American Society for Metals, OH, 1973, p. 10.
[16] D.A. Elkington, R. Wilson, in: P.J. Lloyd (Ed.), Particle Size Analysis, Wiley, New York, 1987, p. 261.
[17] T.R. Mahalingam, in: S.K. Aggarwal, H.C. Jain (Eds.), Introduction to Mass Spectrometry, Indian Society for Mass Spectrometry, 1997, p. 13.
[18] S. Vijayalakshmi, R. Krishna Prabhu, T.R. Mahalingam, C.K. Mathews, At. Spectrosc. 132 (1992) 61.
[19] National Bur. Stand. (US), Monogr. 25, 18 (1981) 72.
[20] M. Kamruddin, P.K. Ajikumar, S. Dash, B. Purniah, A.K. Tyagi, K. Krishan, Instrum. Sci. Technol. 23 (2) (1995) 123.
[21] M. Kamruddin, P.K. Ajikumar, S. Dash, R. Krishnan, A.K. Tyagi, K. Krishan, J. Thermal Anal. 48 (1997) 277.
[22] S. Dash, M. Kamruddin, A.K. Tyagi, Bull. Mater. Sci. 20 (3) (1997) 359.
[23] M. Tischler, M.J. Koremblit, in: Temperature: Its measurement and control in Science and Industry, vol. 5, Part 1. Thermodynamic Methods, Scales, Fixed Points, Radiation Thermometry, American Institute of Physics, New York, 1982, p. 383.
[24] M.I. Pope, M.D. Judd, Differential Thermal Analysis: A Guide to the Technique and Application, Chapter 5: Phase transition, Heyden, London, 1977, p. 44.
[25] W.W. Wendlandt, Thermal Methods of Analysis, Wiley, New York, 1974, p. 29.
[26] G.V.N. Rao, V.S. Sastry, H.S.G.K. Murthy, V. Seshagiri, T.S. Radhakrishnan, Powder Diffraction 11 (3) (1996) 200.
[27] Goutam Ghosh, PhD Thesis, University of Madras, 1998, p. 30.
[28] B.D. Cullity, Elements of X-ray Diffraction, Addison-Wesley, Reading, MA, 1956, p. 99.
[29] J.C. Fuggle, A.F. Burr, L.M. Watson, D.J. Fabian, W. Long, J. Phys. F 4 (1974) 337.
[30] J. Sestak, V. Satava, W.W. Wendlandt, Thermochim. Acta 7 (1973) 332.
[31] M.E. Brown, Introduction to Thermal Analysis, Chapman & Hall, London, 1988, p. 127.

[32] A.K. Galway, Chemistry of Solids, Chapman and Hall, London, 1967, p. 192.
[33] S. Dash, M. Kamruddin, P.K. Ajikumar, R. Krishnan, A.K. Tyagi, Indian J. Chem. Technol. 5 (1998) 35.
[34] T. Ueki, A. Zalkin, D.H. Templeton, Acta Crystallogr. 20 (1966) 836.
[35] M. Kamruddin, P.K. Ajikumar, S. Dash, R. Krishnan, A.K. Tyagi, K. Krishan, Thermochim. Acta 287 (1996) 13.
[36] J.C. Taylor, M.H. Mueller, R.L. Hitterman, Acta Crystallogr. 20 (1966) 842.
[37] P.D. Garn, Thermoanalytical Methods of Investigation, Academic Press, New York, 1965, p. 247.
[38] R.A. Nyquist, R.O. Kayel, Handbook of Infra-red and Raman Spectra of Inorganic Compounds, vol. 4, Compound No. 191, Academic Press, San Diego, CA, 1997, p. 143.
[39] K. Nakamoto, Infra-Red and Raman Spectra of Inorganic and Coordination Compounds, 3rd Ed., Wiley, New York, 1963, p. 227.
[40] D. Brown, in: K.W. Bgnall, H.J. Emeleus (Eds.), Inorganic Chemistry, Series 2, vol. 7, Butterworths, London, 1975, p. 145.
[41] J.R. Ferraro, A. Walker, J. Chem. Phys. 42 (1965) 1278.
[42] S. Dash, M. Kamruddin, S. Bera, P.K. Ajikumar, A.K. Tyagi, S.V. Narasimhan, Baldev Raj, J. Nucl. Mater. 264 (1999) 271.
[43] G. Lundgren, Ark. Kemi 2 (1951) 535.
[44] G. Lundgren, L.G. Sillon, Ark. Kemi 1 (1949) 277.
[45] F. Vratny, S. Kern, F. Gugliotta, J. Inorg. Nucl. Chem. 17 (1961) 281.
[46] Anne-Gobichon Gobichon, Jean-Paul Auffredic, Daniel Louer, Solid State Ionics 93 (1997) 51.
[47] H. Leigh, E. Mc Cartney, J. Am. Ceram. Soc. 57 (1974) 192.
[48] B.W. Veal, D.J. Lam, H. Diamond, H.R. Hoekstra, Phys. Rev. B 15 (6) (1977) 2929.
[49] C.D. Wagner, W.M. Riggs, L.E David, J.F. Mouder, G.E. Mailenberg (Eds.), Handbook of X-ray Photoelectron Spectroscopy, Perkin–Elmer, Eden, Prairie, MN, 1979.
[50] B.W. Veal, D.J. Lam, Phys. Rev. B 10 (12) (1974) 4902.
[51] B.W. Veal, D.J. Lam, in: Gmelins Handbook of Inorganic Chemistry, A 5, Verlag Chemie, Weinheim, 1973, p. 177.